LARA: a Lagrangian Reanalysis based on ERA5 spanning from 1940 to 2023

Lucie Bakels[1,2], Michael Blaschek[1], Marina Dütsch[1], Andreas Plach[1], Vincent Lechner[1], Georg Brack[1], Leopold Haimberger[1], and Andreas Stohl[1]

[1]Department of Meteorology and Geophysics, University of Vienna, Vienna, Austria
[2]Stockholm Resilience Centre, Stockholm University, Sweden

Correspondence: Lucie Bakels (lucie.bakels@su.se)

Abstract. Meteorological reanalyses are crucial datasets in atmospheric research, providing the foundation for many scientific applications. However, most reanalyses follow a Eulerian framework, providing data at specific, fixed points in space and time. This fixed-location approach is suitable for many scientific analyses, but studies focused on transport in the atmosphere would benefit from a Lagrangian framework, which provides data along dynamic, continuous trajectories following the movement of air.

To achieve this, the Lagrangian particle dispersion model FLEXPART was driven off-line with data from ECMWF's (European Centre for Medium-Range Weather Forecasts) latest reanalysis, ERA5, to convert the Eulerian ERA5 data into a Lagrangian format. FLEXPART utilises the grid-scale winds from ERA5 and stochastic parameterisations of turbulence and convection to advect particles in a domain-filling mode, where the global atmosphere is represented by 6 million particles that move freely in the atmosphere, with their number density following closely the density of air. The resulting new Lagrangian Reanalysis (LARA) dataset has been stored in an easily searchable database and made accessible to researchers all over the world. It will enable a wide range of studies, including global and regional analyses of extreme events, water and energy transport in the atmosphere, and atmospheric energy budgets.

Here, we describe the data format, and how the data can be accessed and analysed. Using four examples, we give a non-exhaustive list of possible applications for which LARA could be used for. We show methods for how the evolution of air masses and their properties can be studied, and how climatologies can be established. Our examples include a study of the evolution of the Hadley cell circulation, a climatology of warm conveyor belt events, a measure of continentality ~~by~~ based on the time it takes for air to reach land from the ocean, and an evaluation of the dynamical consistency between subsequent ERA5 meteorological fields.

1 Introduction

In order to forecast the future state of the atmosphere with a numerical model that solves the prognostic equations of motion, the atmosphere's initial state must be known with high accuracy. To describe this initial state, meteorological observations are essential. However, these measurements contain errors, have incomplete spatiotemporal coverage, and an analysis of the

initial state of the atmosphere based on observations alone (e.g., through simple interpolation) would contain dynamical in-
25 consistencies. Therefore, the observations are usually merged with a Eulerian model forecast from a previous analysis using
sophisticated data assimilation methods (e.g. Courtier and Talagrand, 1987). The product of such a data assimilation system is
a Eulerian representation of the atmosphere, in which the atmospheric state variables are provided at fixed locations in space
and time. These analysis data represent our best estimate of the state of the atmosphere at the given time, ideally also including
an estimate of uncertainty (e.g., through ensemble methods).

30 Time series of such analyses can be used for meteorological case studies. However, since weather forecast models change
with time, long series of operational analyses are not well suited for the analysis of climate variability or trends, or the con-
sistent comparison of different events. For such purposes, so-called reanalyses have been produced using models and data
assimilation systems that are "frozen" over the reanalysis period, the longest of which span more than a millennium (Last Mil-
lenium Reanalysis by Hakim et al., 2016). Several agencies have produced reanalyses, including the Climate Forecast System
35 Reanalysis (CFSR), created by the American National Centers for Environmental Prediction (NCEP) (Saha et al., 2010), the
Modern-Era Retrospective analysis for Research and Applications (MERRA and MERRA-2), created by the American Na-
tional Aeronautics and Space Administration (NASA) (Rienecker et al., 2011)(Rienecker et al., 2011; Gelaro et al., 2017), the
Japanese 55-year and 75-year Reanalysis (JRA-55 and JRA-3Q, respectively), created by the Japanese Meteorological Agency
(JMA) (Kobayashi et al., 2015)(Kobayashi et al., 2015; KOSAKA et al., 2024), and the ECMWF Reanalysis v5 (ERA5), cre-
40 ated by the European Centre for Medium-Range Weather Forecasts (ECMWF) (Hersbach et al., 2020). Notwithstanding the
fact that also reanalyses contain inhomogeneities resulting from changes in the observation system (e.g. Sterl, 2004) and
differences exist between the reanalyses (e.g. Fujiwara et al., 2017), they are an extremely rich source of information for scien-
tists from many different disciplines and support a wide range of scientific inquiries. These datasets offer a comprehensive view
of the atmosphere, integrating observations and model data to generate consistent and accurate historical records of meteoro-
45 logical conditions. Such reanalyses are indispensable for understanding weather patterns, climate variability, and atmospheric
processes, and modern reanalyses also include ocean and land components.

Traditional reanalyses are all Eulerian, delivering data at fixed spatial locations. While this stationary framework is effective
for many applications, it poses limitations for studies that require understanding the movement of air or its trace constituents.
A Lagrangian translation, which tracks data along continuous trajectories (Stohl, 1998), addresses this gap. This approach is
50 particularly beneficial for research focused on atmospheric transport processes and source-receptor relationships (SRR), where
following the path of air parcels provides deeper insights into phenomena such as pollutant dispersion, greenhouse gas budgets,
moisture and energy transport, or the structure of synoptic systems.

Studies that utilise the Lagrangian tracing of air parcels are plentiful, however, they are often restricted to case studies, or
transport climatologies for specific sites or certain processes. For instance, Wernli and Davies (1997a) and Wernli et al. (2002)
55 used trajectory calculations to explore dynamical aspects of cyclones; Stohl (2001) and Eckhardt et al. (2004) established
climatologies of warm conveyor belts and other mid-latitude air streamsairstreams; Dirmeyer and Brubaker (1999) studied
evaporative moisture sources; Zschenderlein et al. (2019) examined processes determining heat waves; Stohl et al. (2003) and
Sprenger and Wernli (2003) quantified stratosphere-troposphere exchange fluxes; and Stohl et al. (2002) characterized the

pathways and time scales of intercontinental pollution transport. Each of these studies calculated their own set of Lagrangian
trajectories for the specific period and region of interest to that study. This constitutes a considerable effort and requires
specialized expertise, since it is necessary to produce or download the Eulerian meteorological input data and run the trajectory
model before it is possible to proceed with the analysis of interest. An alternative to this is to produce a global dataset of
continuous trajectories that fill the entire atmosphere and are tracked over a long time period.

Stohl and James (2004, 2005) were the first to produce such a dataset, for the purpose of studying the atmospheric branch of
the global water cycle. They discretised the entire atmosphere using air "particles" of equal mass and calculated their trajectories using FLEXPART (Stohl et al., 1998a) driven by ECMWF operational analyses. The original purpose of this methodology
was to diagnose atmospheric moisture transport by establishing a connection between regions of net evaporation and regions
of net precipitation. They validated their method using an extreme precipitation event and identified the regions from which
the precipitation originated. Several other studies have used a similar approach for quantifying source-sink relationships of
water (e.g. Nieto et al., 2006; Gimeno et al., 2010; Chen et al., 2012). Läderach and Sodemann (2016) simulated the period between 1979 and 2013 using data from the ECMWF ~~ERAInterim~~ ERA-Interim reanalysis and used a moisture source diagnostic
(Sodemann et al., 2008) to quantify the atmospheric residence time of water vapour. ~~Their dataset is available on request.~~ Reithmeier and Sausen (2002) calculated domain-filling trajectories online in a climate model, and Vázquez et al. (2024) produced
a dataset of 30 million FLEXPART trajectories with a temporal resolution of 3 hours, based on the ECMWF ERA5 reanalysis
for the period 1980-2023~~, available upon request~~. This dataset was produced with FLEXPART version 10.4 (Pisso et al., 2019).
Since then, a new version of FLEXPART (version 11) has been released, showing a large decrease in particle distribution
degradation in the troposphere over time, where in version 10.4, the particle number density does not well represent air density
after some time (Bakels et al., 2024). This new version also allows for the output of temporal-averaged properties, allowing for
a more complete representation of the path of air through the atmosphere. Therefore, here we present an open-access general-
purpose dataset of global domain-filling trajectories using these latest features of FLEXPART and covering the full period of
~~1940-2024~~ January 1940 until March 2024 using the ERA5 reanalysis.

In this work, we present a global dataset that may be called a Lagrangian reanalysis (LARA). It provides the hourly positions
of six million particles whose trajectories were calculated using the latest FLEXPART version ~~(11)~~(Bakels et al., 2024), driven
by the ECMWF ERA5 reanalysis from 1940 to March 2024 (Hersbach et al., 2020). Meteorological data are provided at the
particle locations, which can be used for a wide range of possible analyses. The dataset is open-access and is stored in ~~ZARR~~
Zarr data format (doi: https://phaidra.univie.ac.at/o:2121554). This paper describes the dataset production, its limitations, and
gives four examples of possible applications. We demonstrate how the dataset can be used to trace air mass transport, how
to identify certain dynamical phenomena, such as warm conveyor belts, and how to diagnose properties of the underlying
Eulerian reanalysis data. All analyses and plotting routines are provided in the supplement and can be used as templates for
further explorations. A first application of a preliminary version of this dataset was presented by Baier et al. (2022) who
used it to examine the transport of moisture and energy from the tropical Pacific and its relationship to the El Niño/Southern
Oscillation (ENSO).

2 Methods

2.1 Input data

For the creation of the LARA dataset, we used the most recent reanalysis dataset of ECMWF, ERA5 (Hersbach et al., 2020), with ~~hourly~~ its native hourly temporal and 137-level vertical resolution and a reduced horizontal resolution of 0.5° × 0.5° ~~data as input on 137 vertical model levels, of which 88 are located below 20 km.~~due to storage constraints.ERA5 is a widely used global atmospheric reanalysis dataset that provides detailed hourly estimates of atmospheric, land, and oceanic variables, covering the period from 1940 to the present. ERA5 combines vast amounts of historical observational data with advanced modelling and data assimilation techniques, ensuring high temporal and spatial resolution and a high level of consistency. It is built on ECMWF's Integrated Forecast System (IFS) Cy41r2, using 4D-Var data assimilation to incorporate a wide range of observational data, including satellite observations and in-situ measurements. ERA5 uses a consistent model framework over the whole reanalysis period. However, the observation system has changed tremendously over this period, and thus the assimilation of observation may lead to spurious variability and trends in certain variables. Such artifacts may extend to the LARA data set, such that care should be taken when applying trend analyses. Table 1 lists the ERA5 input parameters used for producing our dataset. The ERA5 data were obtained from the ECMWF archives using the flex_extract software (Tipka et al., 2020).

2.2 FLEXPART

FLEXPART is a Lagrangian Particle Dispersion Model (LPDM) that advances particles by interpolating gridded meteorological data from ECMWF or NCEP to the particle positions and applying a numerical trajectory calculation scheme. The input data include grid-scale three-dimensional fields of wind velocities, temperature, specific humidity, as well as several surface fields (see Table 1). Particles can be initialised in separate releases or in a domain-filling mode, which discretises the full atmosphere into particles of equal mass. The particles are initialised such that their number density is proportional to the density of air, and each of them represents an equal fraction of the total atmospheric mass. Particles can then be traced forward or backwards in time. FLEXPART trajectories are based on interpolated gridded winds and stochastic parameterisations of sub-grid convection and turbulence. This means that particles move with the large-scale winds with stochastic motions superimposed. FLEXPART uses a first order Euler method in addition to a Petterssen correction (Petterssen, 1940) for advancing particles. FLEXPART also uses the input meteorological data to calculate various derived variables, such as potential vorticity and the height of the tropopause. FLEXPART has a well-documented history (Stohl et al., 1998a, 2005; Pisso et al., 2019), and recently saw a new release by Bakels et al. (2024), which includes a live documentation that records any new additions and changes (https://flexpart.img.univie.ac.at/docs/). Therefore, we refer to Bakels et al. (2024) for a general description of FLEXPART's functionalities but highlight those additions that were specifically implemented in FLEXPART 11 for the creation of the LARA dataset.

Many improvements made in FLEXPART 11 were designed to address challenges encountered during multi-year simulations using the domain-filling option. For example, using the native η coordinates instead of internally transforming all meteorolog-

Table 1. List of ERA5 input variables used in the creation of the LARA dataset. Note that FLEXPART reads in more meteorological parameters, which are needed for simulating additional processes such as wet and dry deposition of chemical substances. However, these were not accounted for here and are thus not listed.

Variable	~~Short~~ ERA5 short name	unit
3D fields		
U and V component of wind	u and v	$\mathrm{ms^{-1}}$
Eta-coordinate vertical velocity	etadot	$\mathrm{s^{-1}}$ ~~(internally:)~~ [*]
Temperature	t	K
Specific humidity	q	kg/kg
2D fields		
U and V component of wind at 10m level	u10 and v10	m/s
Surface pressure	sp	Pa
2 metre temperature	2t	K
2 metre dew point	2d	K
Sensible heat flux	sshf	$\mathrm{W\,m^{-2}}$ ~~(de-accumulated by flex_extract)~~ [**]
Eastward and Northward turbulent surface stress	ewss and nsss	$\mathrm{N\,m^{-2}\,s}$
Geopotential	z	$\mathrm{m^2s^{-2}}$ ~~(converted to topography in above sea-level by flex_extract)~~ [***]
Standard deviation of orography	sdor	m

[*] converted to $\mathrm{Pa\,s^{-1}}$ by flex_extract, [**] de-accumulated by flex_extract, [***] converted to topography in m above sea-level by flex_extract

ical data to a vertical coordinate system in units of metres, reduced interpolation errors, and improved the compliance with the well-mixed criterion across most of the atmosphere (Thomson, 1987, Section 3.1). The initial distribution of particles within the domain-filling option was improved to better represent air density throughout the entire atmosphere. Furthermore, introducing OpenMP parallelisation decreased the computing time for our specific application by 75 % as compared to the earlier
130   MPI parallelisation present in FLEXPART 10.4 (Pisso et al., 2019).

2.3 Set-up

For our purpose we used the domain-filling option, which makes it possible to discretise the whole atmospheric mass into a set of particles, which can be traced both forward and backward in time. Here, we traced the particles forward in time. We used 6 million particles, with equal mass, that are initially positioned in the full atmosphere such that the particle density is
135   proportional to the air density. This means that each particle represents a fixed air mass of approximately 0.86×10^{12} kg of air, but depending on where it moves, its represented volume of air may change (larger volumes where the air density is lower). A $1° \times 1°$ column on the equator contains approximately 300 particles at any point in time.

The dataset spans the period of 1940 to 2023. Given that the ~~full period from start to finish~~ calculations for the full period would take over a year to complete, and given the progressive particle distribution degradation that occurs during extended runs (Bakels et al., 2024) (see also ~~section~~Section 3.1), we divided the full period in twelve streams of eight years, with an overlap of one full year for each period. ~~The three-month~~ Particles cannot be traced beyond the eight years. Therefore, the full year overlap between the different computational streams guarantees that, in post-processing analyses, for every instance in time during the entire LARA period, particles can be traced both forward and backward in time, as long as the desired duration of tracking is shorter than ~~3 months~~1 year.

The trajectories were calculated with a numerical integration time step of 300 seconds. We found that particle densities ~~deviate by approximately 20% less from~~ show smaller deviations, with a reduction of the difference of particle mass densities to ERA5 air densities of approximately 20% when using 300 seconds time steps compared to 600 second time steps. A further reduction of the time step did not result in a level of improvement that would justify the increase in run-time. However, to ensure correct particle behaviour, much shorter adaptive time steps were used in the turbulent atmospheric boundary layer; 10% (1%) of the variable Lagrangian time scale for horizontal (vertical) motions. This corresponds to the following FLEXPART options:`CTL=10` and `IFINE=10` (see Bakels et al., 2024, for details). The dataset is large, with a total size of approximately 320 TB, and making it openly available constrained our choice of total particle number and temporal output resolution. Section 3.2 describes possible limitations on the use of the dataset due to its resolution.

For the simulations, we used the Vienna Scientific Cluster 5 (VSC-5) AMD EPYC Milan compute nodes, which have 2×64 cores and 256 threads in total, and 512 GB RAM. We used the GNU Fortran compiler (GCC 12.2.0)~~with the following optimisation flags: -O3 and -march=native.For the best use of non-uniform access (NUMA), we set `export OMP_PLACES=cores` and `export OMP_PROC_BIND=true`.~~In total, running all 12 ~~seven-year~~ eight-year periods took approximately 290000 cpu-hours and a total of 32 days to complete.

2.4   The LARA dataset

The LARA data set consists of hourly particle output for the entire 84-year period (1940-2023). Table 2 lists the different variables contained in the LARA dataset. Both instantaneous values at the output time as well as hourly values averaged along the trajectories are available for their positions, potential vorticity, specific humidity, air density, temperature, and pressure. Averaged values contain the mean of all instantaneous values produced at each integration time step ($300\,\mathrm{s}$) of the previous hour. The atmospheric boundary layer height, tropopause height, and topography do not have a vertical dimension like the previous listed fields. Therefore, to conserve storage space, these are saved as two-dimensional spatial gridded fields, with an extra time dimension for the atmospheric boundary layer and tropopause height. ~~If users want these variables at the particle positions, they need to interpolate them~~These gridded variables can easily be interpolated to the horizontal particle positions. The topography is taken from ERA5, the atmospheric boundary layer height is computed with the method of Vogelezang and Holtslag (1996) based on the critical Richardson number, and the tropopause height is defined as the first stable layer to fulfill the thermal tropopause criterion (i.e. the vertical temperature gradient is smaller than $0.002\ \mathrm{K\ km^{-1}}$).

Table 2. List of the variables contained within the LARA dataset. The dimensions are defined at the top of the list, followed by a series of variables with the dimensions particle index and time. Lastly, meteorological data lacking a third spatial dimension is stored as a grid.

	Short name	~~unit~~Unit
Dimensions		
Particle index (1 – 6 million)	`particle`	index
Gregorian time	`time`	\<YYYY-MM-DD\>T\<HH:MM:SS\>
Gridded longitude (0,360,0.5)	`longitude`	degree east
Gridded latitude (-90,90,0.5)	`latitude`	degree north
Particle data variables (`particle`, `time`)		
Longitude	`lon`	degree east
Longitude average	`lon_av`	degree east
Latitude	`lat`	degree north
Latitude average	`lat_av`	degree north
Height	`z`	metre above ground
Height average	`z_av`	metre above ground
Potential vorticity	`pv`	pvu
Potential vorticity average	`pv_av`	pvu
Specific humidity	`sh`	$\mathrm{kg\,kg^{-1}}$
Specific humidity average	`sh_av`	$\mathrm{kg\,kg^{-1}}$
Density	`rho`	$\mathrm{kg\,m^{-3}}$
Density average	`rho_av`	$\mathrm{kg\,m^{-3}}$
Temperature	`T`	K
Temperature average	`T_av`	K
Pressure	`prs`	Pa
Pressure average	`prs_av`	Pa
Gridded data variables (`latitude`, `longitude`, `time`)		
Atmospheric boundary layer height	`hmix`	metre above ground
Tropopause height	`tro`	metre above ground
Gridded data variable (`latitude`, `longitude`)		
Topography	`to`	metre above sea level

As stated before, the dataset spans the period of 1940 to March 2024, and is divided into chunks of eight years, with an overlap of one year. Data is initially written in NetCDF by FLEXPART, but converted and stored in monthly ~~zarr~~ Zarr files, organised as follows: `<PERIOD>` / `<YEAR>` / `<MONTH>` / `<VARIABLE>`. For example, the instantaneous temperature in January of 1944 is located in `1940-1947/1944/01/T`. Zarr is a cloud-friendly data format implemented in Python that stores chunked, compressed multi-dimensional arrays. Zarr offers better compressibility and access than NetCDF and is accessible using Python's package xarray (Hoyer and Hamman, 2017) (at least since v2022.12.0). Using xarray and the default compressor `Blosc(cname='lz4', clevel=5,shuffle,blocksize=0)` for ~~zarr~~ Zarr results in a size reduction of $\sim 15\%$ as opposed to using the default NetCDF `zlib` compressor. Opening and using ~~zarr~~ Zarr files with xarray is nearly identical to using NetCDF files, but, for example, opening ~~a month's worth of files normalised per variable~~ files is $\sim 60\%$ faster. Loading one day of data for one variable into memory is $\sim 80\%$ faster using ~~zarr~~ Zarr than using NetCDF.

The following Python code example shows how to retrieve one variable for one month and store it locally.

```
 1: # using \DIFdelbegin \DIFdel{zarr }\DIFdelend \DIFaddbegin \DIFadd{Zarr }\DIFaddend version 2.9 or
                                                     later, but lower than 3
 2: import zarr
 3: import xarray as xr
 4: # open the remote dataset
 5: ds = xr.open_zarr("https://data.eodc.eu/collections/LARA/2017-2024/2023/01/T")
 6: # print
 7: print(ds)
 8: <xarray.Dataset>
 9: Dimensions:    (particle: 5914326, time: 744)
10: Coordinates:
11: * particle   (particle) int32 1 2 3 4 5 ... 5914323 5914324 5914325 5914326
12: * time       (time) datetime64[ns] 2023-01-01 ... 2023-01-31T23:00:00
13: Data variables:
14: T          (particle, time) float32 ...
15: # example size: 18GB (one month)
16: # store locally (\DIFdelbegin \DIFdel{zarr}\DIFdelend \DIFaddbegin \DIFadd{Zarr}\DIFaddend , netcdf,
                                                     pandas, ...)
17: ds.to_zarr("/path/on/your/machine/LARA-2017-2024-202301-T")
18: ds.to_netcdf("/path/on/your/machine/LARA-2017-2024-202301-T.nc")
```

3 Validation and limitations of LARA

In this section, we validate the dataset using the well-mixed condition (Section 3.1), and describe (potential) limitations in using LARA (Section 3.2). Since ground truth trajectories are not available for the entire LARA period across all atmospheric layers, it is not possible to make an absolute quantification of errors. However, using quasi-conservative properties (e.g. PV), it is possible to show differences between methods, and to highlight additional errors made during the transition periods between ERA5 12-hourly assimilation windows. Using the same parameters as those used to create LARA, ~~section~~ Section
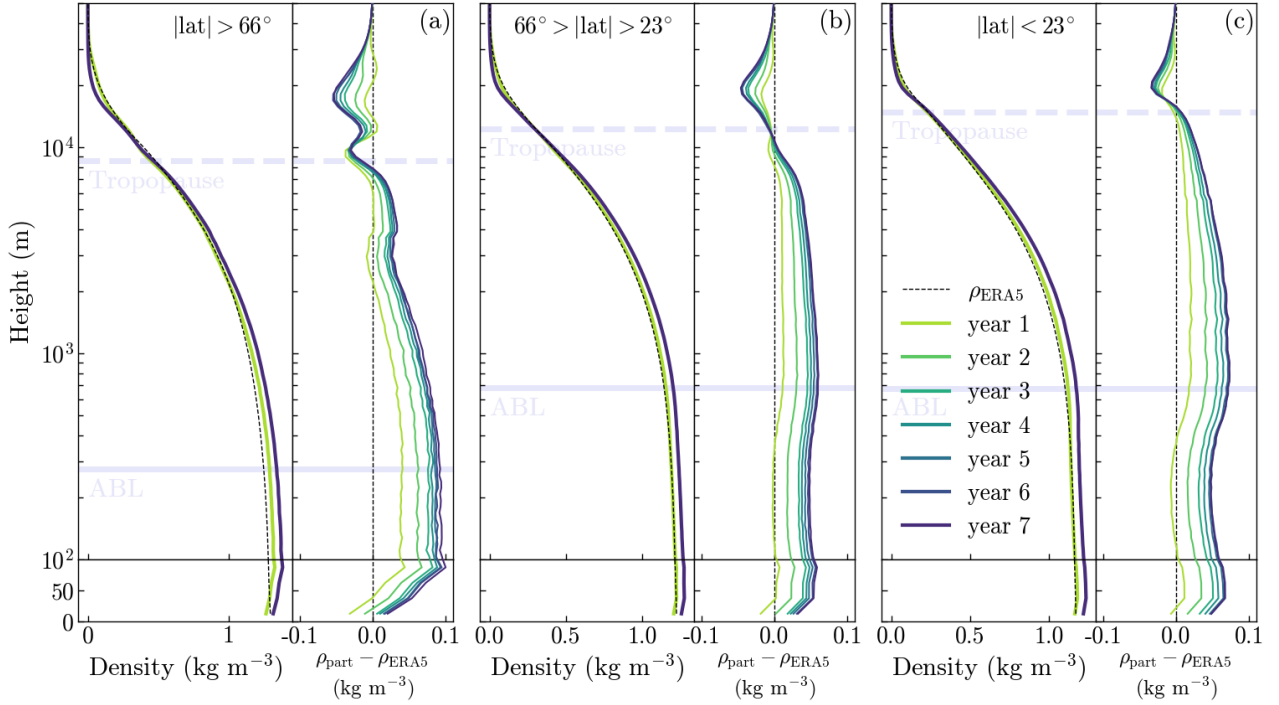
Figure 1. Density distribution of particles as compared to the density of air given by the ERA5 data. Each line represents the averaged density of every hour in the seventh month (July) of consecutive years after the start in January of the twelve simulations covering the 84-year period. Initially, the simulations start with a perfectly fitting particle density distribution that corresponds exactly to the air density profile. The results are separated into three regions: Polar regions (**a**), mid latitudes (**b**), and the tropics (**c**).

3.2 of Bakels et al. (2024) shows that in 2020, below 10 km, errors due to assimilation window transitions are negligible as compared to other errors. Using the improved interpolation scheme of FLEXPART 11, which removed an interpolation step by advancing particles using the native vertical coordinate grid of the ERA5 data, a reduction of $\sim 15\%$ and $\sim 8\%$ in PV errors is observed above 10 km and between 5-10 km, respectively. FLEXPART shows generally good agreement with tracer experiments (ETEX and CAPTEX), with Spearman coefficients of tracer concentrations between 0.56-0.68. More details on FLEXPART 11 improvements can be found in Bakels et al. (2024).

3.1 Density distribution

The so-called well-mixed condition (Thomson, 1987) states that particles of a passive tracer that are initially well mixed in position must remain so throughout the simulation. This is an important criterion to judge the quality of a Lagrangian model simulation which, however, is often quite difficult to achieve in practice. While turbulent schemes have been developed to fulfill this criterion well on short time scales in the boundary layer (including the turbulence scheme implemented in FLEXPART),

few global models were tested on long time scales. Deviations from well-mixedness can arise due to mass inconsistencies in the meteorological input data, interpolation errors, numerical errors, or errors in the convection or turbulence schemes.

Despite the modifications made to improve FLEXPART's adherence to the well-mixed condition, specifically the removal of an interpolation step by using the native η coordinates within FLEXPART 11 (Bakels et al., 2024), as discussed in that study, and using a rather short maximum time step of 300 seconds when producing the LARA dataset, the condition was not entirely fulfilled. Following the method described in Cassiani et al. (2015), ~~Fig.~~ Figure 1 shows the degradation of the vertical particle density profile as compared to the ERA5 air density profile within the LARA dataset over time. Our comparison is conducted on a $0.5° \times 0.5°$ grid with 4 linear vertical levels below 100 m and 100 logarithmically spaced vertical levels between 100 m and 10 km. The different colours represent the mean July profiles, averaged over all twelve simulation streams, one to seven years after their start. We find similar patterns for all 7-year simulation streams and thus only show the average over the twelve simulation streams. The degradation rate is initially rapid, weakens after the third year and eventually stabilises around the fifth year. During the seventh year, below the tropopause we find height-weighted overdensities of about 3.5-6.6 % in our data, which corresponds to an accumulation of particles in the troposphere; in the stratosphere, the sign is reversed (-65 %), indicating a lack of particles there. Tests showed that these deviations are not caused by FLEXPART's stochastic turbulence and convection parameterisations but must be due either to small mass inconsistencies in the grid-scale winds, their interpolation, or the numerical trajectory integration. ~~The maximum deviation at any latitudinal-averaged volume is 0.6% of the particles that should be available in that given volume. This volume is located in the upper stratosphere. Despite this relatively low number, there are no particle-free voids, indicating that particles fill the entire atmosphere over the full period of the simulations. This is important because it means that transport climatologies can be established from the LARA dataset for any location of the globe. However, a few words of caution are necessary, especially since deviations at discrete times can be larger.~~

Figure 1 shows that, when air density is calculated from the particle mass in a volume, there can be systematic deviations to the real air density. Therefore, it is always better to take the air density from the ERA5 values interpolated to the particle positions (Table 2: *rho* and *rho_av*), not the mass of the particles. ~~Similarly, when the total transported mass from a specific source or receptor volume is of interest, it may be preferable to avoid using the accumulated mass of the tracked particles. Instead, the mass can be calculated using the average air density within the source or receptor volume.~~ Another potential issue is the use of the dataset for quantitatively studying transport processes on time scales longer than a few months, since there could be small systematic errors in calculated ~~SRRs~~ source receptor relationships (SRRs). This could affect, for instance, the calculation of the age-of-air in the stratosphere from multi-annual particle tracing (e.g. Waugh and Hall, 2002).

3.2 Resolution limitations

For establishing reliable SRRs from the LARA dataset, a large enough number of particles is needed. A single particle cannot correctly characterise a transport pathway, due to the stochastic nature of turbulence and convection. The number of particles needed to obtain statistically significant results depends on the application. For example, to identify the transport pathway to a specific location on a given date, it would be necessary to trace at least a few hundred particles. However, for characterizing the climate-mean transport pathway from or to a certain location, it is not necessary to trace this many particles at every time step.

Since particle density is limited, this also means that the effective space-time resolution of the LARA dataset is limited and that always a certain search volume is needed, from which (or to which) particles can be tracked meaningfully. Since air and
235 particle density decrease with height, larger search volumes are needed at higher altitudes than at lower altitudes. For example, at a single point in time, a $1° \times 1°$ column at the equator contains approximately 300 particles, of which ~ 150 are below 5 km in altitude and only ~ 10 are above 20 km. Therefore, LARA is not suited to determine the dispersion of air from a point source, especially not for individual times. This means that a separate simulation might still be required to obtain the necessary high resolution. Nevertheless, a valuable addition to many such studies would be to have a climatology of the transport over
240 extended periods of time. With our dataset this is possible.

4 Examples

In this section, we present a series of examples of potential applications of the LARA dataset. It should be noted that these examples do not represent the full range of possibilities~~or are fully explored on themselves~~, nor are they investigated in full detail here; however, they are sufficient for giving an understanding of the potential approaches that could be taken. In
245 ~~section~~Section 4.1, we demonstrate how particles and their properties can be selected and traced for an extended period of time. In ~~section~~Section 4.2, we show how atmospheric phenomena can be identified by selecting particles based on their dynamical properties. In ~~section~~Section 4.3 we present a Lagrangian definition of continentality by tracking the time particles spend over land. Finally, in ~~section~~Section 4.4, we illustrate how LARA can be employed as a diagnostic for testing the internal consistency of the ERA5 data. Our first two examples show trends that span the entire LARA period. However, since the
250 quality of LARA is determined by its underlying ERA5 data, we urge caution when examining trends over periods that use different assimilation data.

4.1 Trends in equatorial transport

The response of the Hadley circulation to climate change has been studied extensively in recent decades, utilising a range of methodologies, including reanalysis data (e.g. Stachnik and Schumacher, 2011; Zaplotnik et al., 2022), climate models (e.g.
255 Grise and Davis, 2020), and idealised general circulation models (e.g. Tandon et al., 2013). Figure 2 shows an example of how LARA could aid in further understanding alterations in circulation patterns, exemplified by the Hadley cell. By monitoring the distribution of particles originating from the equator over time, we can identify changes in the circulation properties of the Hadley cell. In this example, we demonstrate one of LARA's fundamental capabilities, namely the quantification of mass transport from selected regions. LARA is able to trace the movement of mass (and energy/moisture, etc.) forward to identify
260 downwind receptor regions, as well as locating upwind sources by tracing particles backward. We selected particles that crossed the equator their first time during March, when the ITCZ is close to the equator (Figure 2a), and traced them forward for 20 days (Figure 2b). This was carried out for each year within the full time span of LARA (1940-2023). ~~The left panel of figure 2~~Figure 2c-e shows the mean distributions over latitude and height for ~~three selected periods (1940-1949, 1977-1986, and 2014-2023~~the complete period (1940-2023), along with their ~~respective standard deviations, to provide insight into the~~
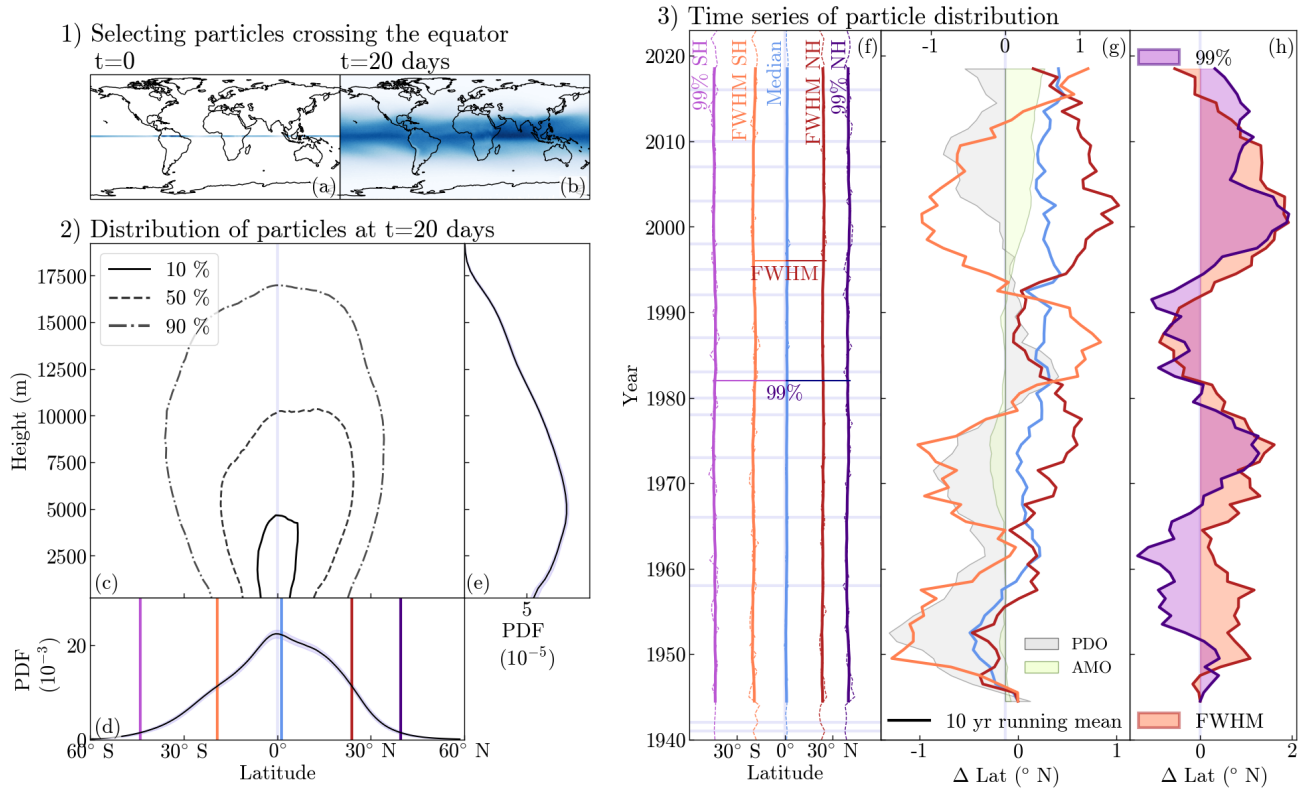
Figure 2. Hadley cell transport of air visualised by the position of particles 20 days after being located on the equator. Distribution of all particles initially positioned on the equator between 0 and 17 km altitude in March within the ~~10-year time periods 1940-1949~~ full LARA period (~~purple~~1940-2023) ~~, 1977-1986~~ at t=0 (~~orange~~a) ~~,~~ and ~~2014-2023~~ after t=20 days (~~green~~b). ~~On the left, the~~ The distribution of all selected particles is plotted over latitude and height (panel ~~a1~~c). Side panels show the probability distribution function (PDF) ~~of each period~~ (~~a2~~ d and ~~a3~~e)~~and how the PDF of the latest and earliest period differ from the middle period (1977-1986) (a4 and a5)~~. Shaded areas denote the standard deviation based on yearly averages~~within each 10 year period~~. The solid vertical lines in panel ~~a2~~ d show the median (blue), full-width-half-maximum (FWHM) on the ~~southern hemisphere~~ Southern Hemisphere (orange), and ~~northern hemisphere~~ Northern Hemisphere (red), and the 99th percentiles on the ~~northern~~ Northern (indigo) and ~~southern~~ Southern (pink) ~~hemisphere~~ Hemisphere averaged over the full 84 year period. Time series of the annual median, FWHM, and 99th percentiles are plotted (dashed lines), together with their 10 year running mean (solid lines), in panel ~~b1~~f. Horizontal lavender lines mark El Niño years. 10-year running ~~mean differences~~ means of changes in the ~~location and the widths, respectively, of the~~ median, FWHM and 99th percentile over time as compared to the mean of the first 10 years are plotted in g and h. g shows the ~~two right-most plots, b2~~ change of the median and ~~b3~~the FWHM separately for the Southern and Northern Hemisphere over time. h shows the change in the full 99th percentile and FWHM (i.e. SH+NH). The 10-year running mean of the Pacific Decadal and Atlantic Multidecadal Oscillations (PDO, AMO) indices for March and April are represented in panel ~~b2~~ g by light gray and light blue patches, respectively, corresponding to the top axis.

265 ~~temporal evolution of mass transport from the equator.For the most recent decade, the vertical distribution of particles after 20 days shows a reduction within the lower parts of the lower atmosphere and an increase at higher altitudes (>4), indicating an amplified rate of mass transport in the vertical direction.~~ PDFs.

As illustrated in panel ~~(a2) by the~~ d by the coloured vertical solid lines, we construct the annual median, full-width-half-maximum (FWHM), and 99th percentile of the particle distribution in panels ~~(b1), (b2), and (b3~~f. Figure 2g shows the change

270 of the median and the FWHM separately for the Southern and Northern Hemisphere over time. Figure 2h shows the change in the full 99th percentile and FWHM (i.e. SH+NH). The dashed lines in all panels represent a 10 year running mean, with the change over time relative to the earliest ~~twenty-year~~ ten-year mean plotted in panel ~~(b2) and (b3)~~g and h. As visible in panel ~~(b2)~~g, the median position of the particles selected in March shifts northwards with time. This could be related to the widening of the Hadley cell in recent decades, which has occurred primarily due to its northward extension in the

275 Northern Hemisphere (Studholme and Gulev, 2018). A higher value of FWHM equates to a circulation pattern that has a broader distribution with a less pronounced peak. Therefore, we use the FWHM as a measure of Hadley cell broadening. Although panel ~~(b3)~~ h shows a wider FWHM during later periods (>1990) in comparison to earlier periods (<1990), the results do not show a progressive broadening trend. Instead, they indicate a cyclical variation. This cyclic pattern may be attributed to the Atlantic Multidecadal Oscillation (AMO), as proposed by Zaplotnik et al. (2022), who found a correlation

280 between a strong AMO and a narrowing of the Hadley cell (i.e. stronger Hadley circulation). The AMO index, provided by https://psl.noaa.gov/data/timeseries/AMO/ ~~(Enfield et al., 2001)~~ (Enfield et al., 2001, last accessed on 26 May 2025) based on the NOAA ~~ERSSTV5~~Extended Reconstructed Sea Surface Temperature version 5 (RSSTV5), only shows a weak relation in the period before 1990, where a negative AMO index roughly corresponds with the broadening of our FWHM (broader and therefore a weaker Hadley circulation). However, there is no such relation visible after the year 1990, where we see a stronger

285 AMO index and a broadening of the Hadley circulation. In contrast, a much more similar pattern over the whole 84 year period can be found in the Pacific Decadal Oscillation (PDO), as provided by https://www.ncei.noaa.gov/access/monitoring/pdo/ ~~(Zhang et al., 1997)~~(Zhang et al., 1997, last accessed on 26 May 2025). Its 10-year running mean shows local peaks around 1952 (minimum), 1971 (minimum), 1982 (maximum) and 2009 (minimum), at similar times of local maxima and minima we observe in the FWHM for the first three extremes. The relation seems to break down around the year 1990, with the last PDO

290 index minimum taking place almost ten years after the local FWHM minimum. ~~This underlines the fact that the Hadley cell circulation is a complicated process in which many factors could be causing anomalies and cannot be solely explained by an index such as the PDO. Therefore, to accurately determine the origin of the observed patterns, it is necessary to divide the globe into~~ To demonstrate the potential of LARA, we only present global results, but it would be interesting to extend the analysis to particular regions (i.e. Pacific, Atlantic, Indian Ocean). ~~Only then can other processesbe investigated using LARA~~This would

295 then allow for the investigation of other processes, e.g. global warming, which has been demonstrated in climate models to result in a broadening of the Hadley cell (e.g. Grise and Davis, 2020).

One of these factors causing anomalies are ENSO events. We illustrate El Niño years by lavender horizontal lines in panel ~~(b1)~~f. If we isolate El Niño years and compute their FWHM, these deviate from the values shown in panel ~~(b3)~~h by only -0.2 degrees on average. However, although following the same trend as the 99th percentile width as shown in ~~(b3)~~h, their

300   99th percentile width is significantly narrower with an average of 2.2 degrees as compared to non-El Niño years. This is in agreement with studies such as Hu et al. (2018), which report a narrowing of the Hadley circulation during El Niño events.

    This example presents an approach that can be readily extended. As we concluded above, it is important to decompose the analysis into different regions. Another example would be to repeat this example for each month of the year, selecting particles along the ITCZ. This could be used to study differences in seasonality, or changing circulations and pathways could be
305 examined by considering the three-dimensional trajectories. Furthermore, it is possible to trace the properties of the transported air, such as its moist static energy and specific humidity.

4.2   Warm conveyor belt events

In this second example, we demonstrate the strength of LARA in using particle dynamics to identify atmospheric phenomena, in this case warm conveyor belts (WCBs). Warm conveyor belts are streams of moist, warm air that ascend ahead of cold fronts
310 in extratropical cyclones, contributing to cloud formation and precipitation. In line with the approach initially taken by Stohl (2001) and Eckhardt et al. (2004), who used trajectory calculations to construct a climatology of WCBs for the 1979-1993 period, we sought to create two 41-year climatologies of WCBs for the periods 1940-1980 and 1981-2021, with a particular focus on the differences in occurrence between the two periods. We adopted one of the selection criteria for finding WCBs as used by Madonna et al. (2014), who studied the period between 1979 and 2010. This criterion states that particles must
315 start at a level below 790 hPa and ascend by at least 500 hPa within a two-day period. The model used in ~~this~~ that study, LAGRANTO (Wernli and Davies, 1997b), does not parameterise convection. Consequently, particles can only rise by large-scale vertical motions. In contrast, in FLEXPART particles can also be lifted by the convection parameterisation, which would lead to erroneous classification of deep convection as WCBs when using only the ascent criterion by Madonna et al. (2014). To prevent this, we also apply the criterion by Eckhardt et al. (2004) that particles need to travel at least $10°$ eastward and
320 $5°$ poleward, which excludes most tropical convection. ~~We also require the~~ Eckhardt et al. (2004) did not use a model that parameterises convection, either. However, when combined with the requirement that the air mass within a WCB ~~per square metre to be larger~~ be greater than 1 kg ~~, implying~~ per square metre —which implies a certain degree of coherence in airstream motion —it reasonably corrects for the erroneous classification of deep convection. However, this did not remove all instances of tropical convection, as visible in ~~figure~~Figure 3. We therefore note that the selection criterion could be improved upon in
325 potential future work.

    Figure 3 reveals similar overall patterns in the different seasons to those observed in earlier studies. Different units were used in earlier studies and we therefore only do a qualitative comparison. They show maxima over the North Pacific and western North Atlantic during NH winter, and east of South America and over the Southern Pacific during NH summer (e.g. Eckhardt et al., 2004; Madonna et al., 2014). We did not identify any WCB events at the foot of the Himalaya during the NH summer, as
330 observed in Madonna et al. (2014). This finding aligns with the results reported by Eckhardt et al. (2004). Madonna et al. (2014) hypothesised that the cause of this discrepancy was the Eckhardt et al. (2004) criterion of trajectories having to move at least $10°$ east and $5°$ north. However, the removal of this criterion did not result in distinctly different patterns in the north of India.
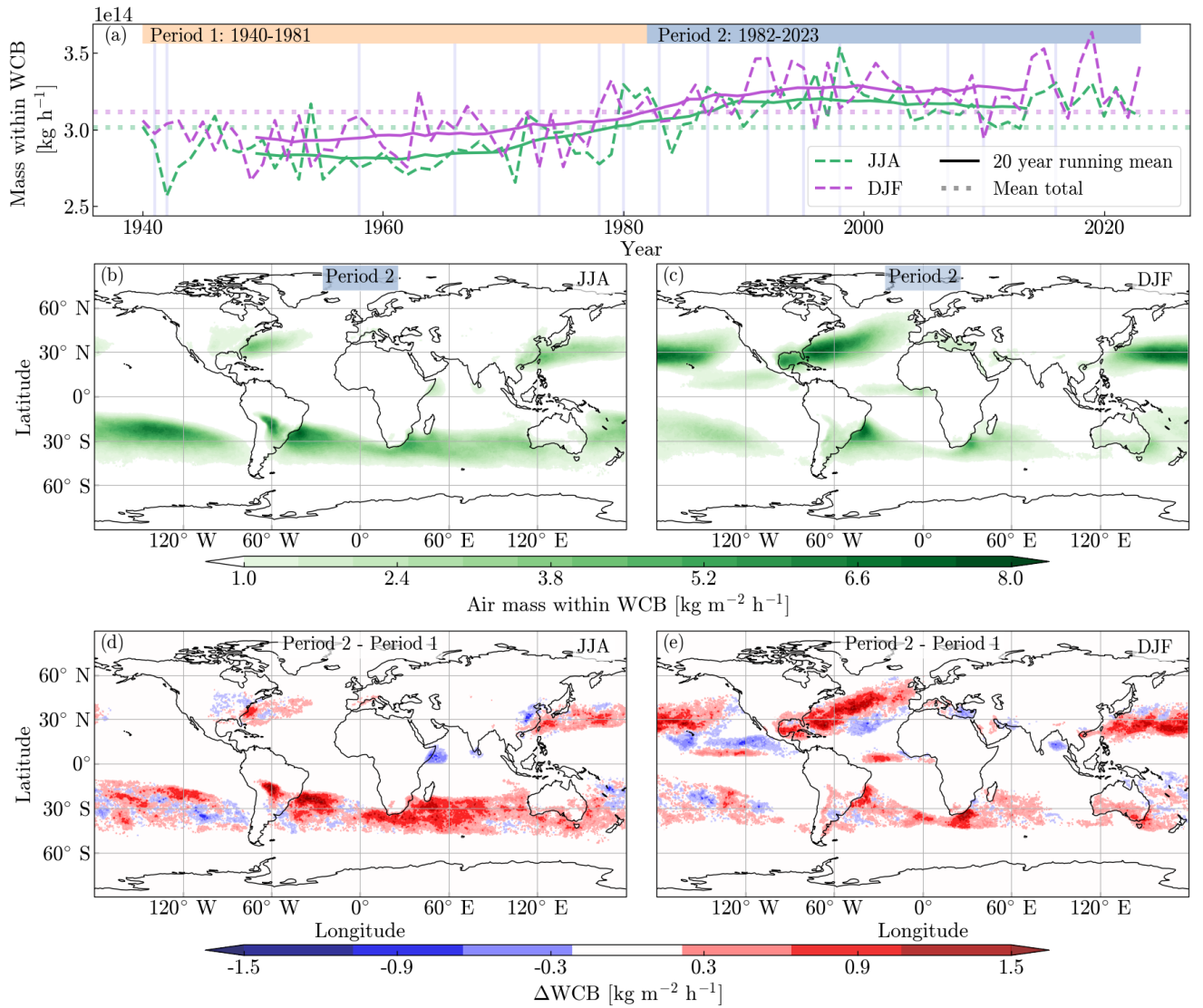
Figure 3. Warm conveyor belt (WCB) climatology. Hourly mean air mass located within WCBs for the months of June, July, and August (green) and December, January, and February (purple)(**a** - dashed lines). 10 year running means and total means are represented by solid and dotted lines, respectively. Horizontal lavender lines mark El Niño years. The middle panels (**b,c**) show the mean hourly air mass located within a WCB for the period between 1981 and 2021, mapped onto the WCB starting points, for JJA (b) and DJF (c). The bottom panels (**d,e**) show the absolute difference between the period 1940-1980, and the period 1981-2021, for JJA (d) and DJF (d). Blue shades indicate a higher WCB incidence during the first 40 years (1940-1980), whereas red shades denotes a higher WCB incidence over the later 40 year period. Particles are selected on a two-day interval basis. All particles that started at a level below 790 hPa and ascended to a level above 500 hPa within the two-day interval are selected. Selected air masses are plotted at the beginning of the two-day selection period (i.e., WCB starting points), mapped on a 0.5° by 0.5° grid, divided by the area surface of their grid cells and averaged over the total number of days within the selection period. A lower limit of 1 kg m^{-2} h^{-1} is set.

We therefore hypothesise that differences in trajectory models, particularly in the treatment of topography, are responsible for this discrepancy.

335   The global total mass within WCBs shows an increase between around 1970 until 1995, whereas we see more or less stable values before and after. The differences between the selected periods separated by 1981, show a broadening of the starting point distribution of WCB events in the more recent period over the South Pacific Ocean during NH summer. An increase of WCB events in the later period seems to occur over the South Atlantic and the Indian Ocean during the NH summer. During the NH winter, we also observe an increase of WCB events in the North Atlantic and North Pacific. However, this appears to be

340 accompanied by a slight north-western shift. During the same period, a slight increase is visible in the western Mediterranean Sea, while a minor decline is discernible in the eastern region. This has the potential to impact precipitation during intense cyclones, as evidenced by Flaounas et al. (2018), whose findings indicate that WCBs contribute up to approximately 50% of the rainfall related to cyclones.

    To study these differences further, the properties of selected WCB air masses, such as potential vorticity and specific hu-

345 midity, along their trajectories could be extracted from LARA. This is beyond the scope of this example, but it could provide further understanding of the factors influencing the changes in WCB occurrence during different periods.

4.3   Continentality of air

Continentality is generally classified by temperature: a contintental climate has at least one month averaging below 0 °C and one above 10 °C according to the Köppen classification (Köppen, 1900). In this last science example, we show a different

350 measure of "continentality", given by the time it takes air to reach land from the ocean. We assigned a timer to each particle that counts the time it spends over land ("travel time"). When the particle is located over land, the timer is incremented by one hour every time step; when the particle is located over the ocean, the timer is reset to zero. To make this timer representative for air-sea interactions, we reset it over the ocean only if the particle is also located in the lowest 1000 m (very roughly corresponding to the atmospheric boundary layer height).

355   In this way we tracked all 6 million particles over the period 2011-2016. As shown in Figure 4, for particles residing in the lowest 1000 m above ground, the resulting travel times are high in Asia and North America, where continental climates are typically found, but also in Africa and South America over the Andes. The highest values are located north of the Tibetan plateau, in a climate that is classified as arid desert (Beck et al., 2023). Generally, continental climates are preferentially found at high latitudes according to the Köppen classification (Beck et al., 2023), whereas our classification also results in long

360 residence times in subtropical desert regions. This shows that the Eulerian measure of continentality (temperature variability) does not always agree with the Lagrangian measure (travel time over land).

    This example could be further explored to measure differences related to seasonality or climate change. For example, the boundary layer height could be used to reset the timer, and better agreement with more classical definitions of continentality could perhaps be obtained by resetting the particle timer only over open water and not over sea ice. Furthermore, moisture

365 tracking could be used to quantify the deposition of oceanic water over the continent by using a moisture tracking diagnostic, such as WaterSip (Sodemann et al., 2008; Fremme and Sodemann, 2019).
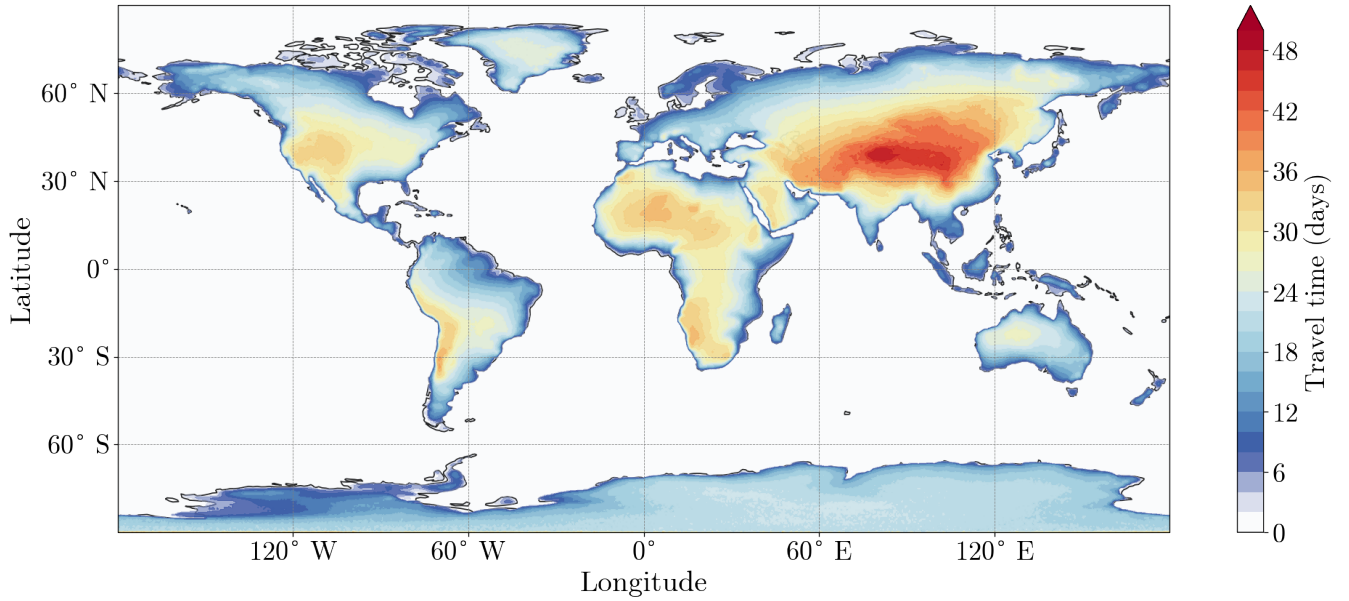
Figure 4. Lagrangian continentality of air. The colors show how many days particles have spent over land or above 1000 m before reaching the respective location. Only particles arriving in the lowest 1000 m are shown.

4.4 Quantifying assimilation errors

The quality of trajectories within LARA is susceptible to interpolation inaccuracies, numerical errors and uncertainties in the turbulence and convection parameterisations, which all in turn result in inaccuracies in the vertical density distribution as shown in ~~section~~Section 3.1. Moreover, since LARA uses wind velocities from the ERA5 reanalysis, the quality of LARA is directly linked to the quality of the ERA5 data, as shown by, e.g., Arnold et al. (2015) who investigated the impact of driving FLEXPART with various datasets. One aspect of the ERA5 data quality is the dynamical consistency of subsequent meteorological fields. Due to the assimilation of observations into ECMWF's IFS model in separate 12-hour time windows, dynamical inconsistencies in time series of the ERA5 data occur especially when switching from one data assimilation interval to the next, resulting in discontinuities in the trajectories. Data assimilation uses available observations and is therefore dependent on both the quality and quantity of such observations (Bell et al., 2021). In addition, different meteorological fields are affected more or less strongly by assimilating different types of observations and therefore the quality of one field does not necessarily guarantee that of others. Due to changes in the observation system, there are also large changes in the quality of the ERA5 data over time. In this final example, we present a methodology for diagnosing the impact of data assimilation on the conservation of semi-conserved tracers along the trajectories throughout the entire ERA5 period. For this, we consider specific humidity, potential vorticity, and potential temperature. These quantities are affected by different physical processes (radiative heating/-cooling, evaporation, etc.) and so are not perfectly conserved in the atmosphere. However, a decent degree of conservation is expected over short time intervals in regions of the atmosphere where diabatic processes are rather slow (i.e., in clear air
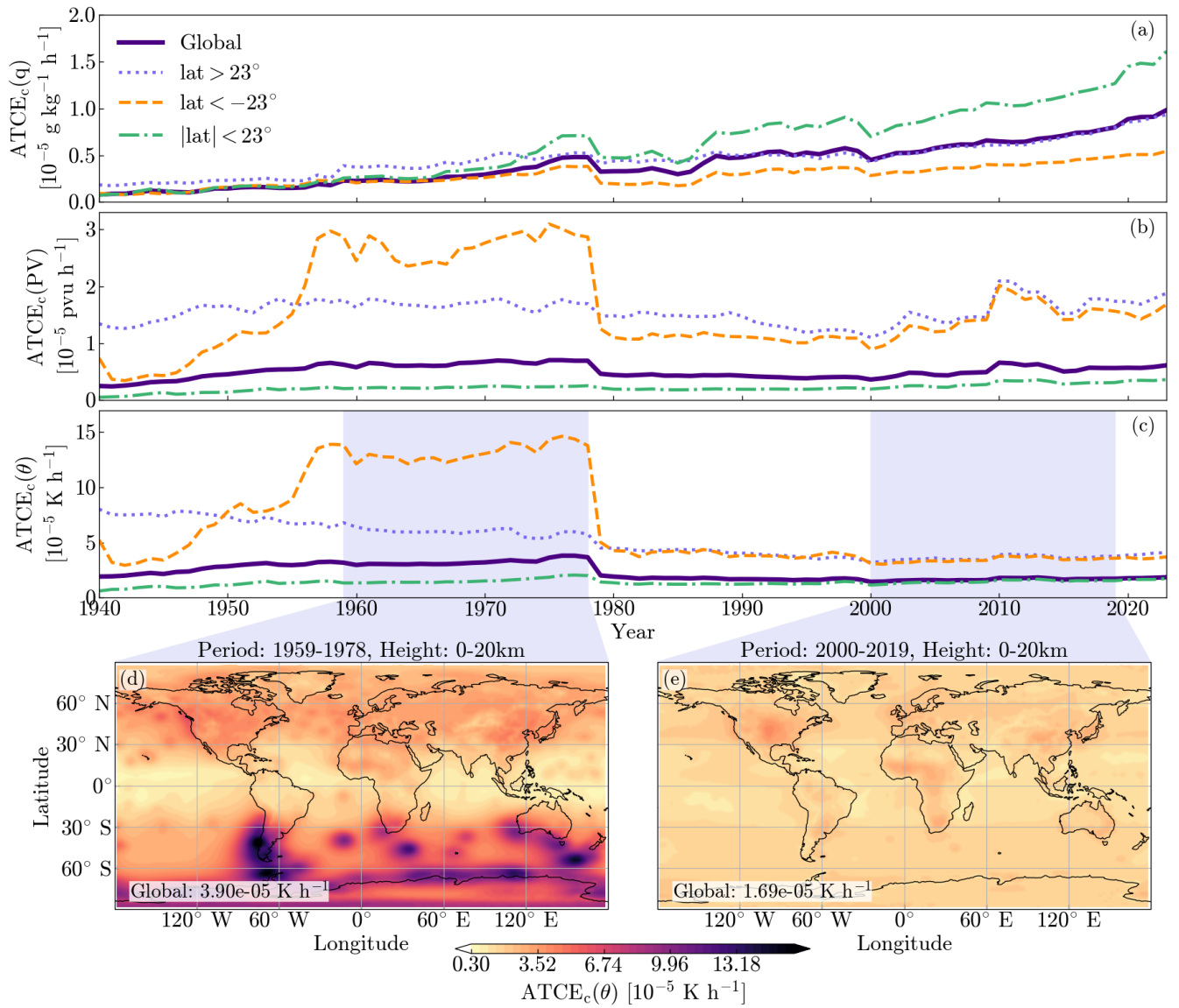
Figure 5. Mean annual absolute baseline-corrected tracer conservation error (ATCE$_c$) of specific humidity (**a**), potential vorticity (**b**), and potential temperature (**c**). Assimilation errors are calculated for particles at altitudes below 20 km using Eq. 3 over the hours when 12-hour assimilation windows change. Results are presented with a baseline subtracted, defined as the mean ATCE of the hours preceding and following the hour when the assimilation window change occurs. The total ATCE (thick purple line) is decomposed into latitudinal regions, namely the Northern Hemisphere north of 23° N (blue dotted line), the Southern Hemisphere south of ~~23~~23° ~~N~~S (yellow dashed line), and the tropics between an absolute latitude of 23 ° N (green dot-dashed line). The mean ATCE$_c$ of potential temperature is mapped on a 2° by 2° grid for the period 1959-1978 (**d**) and for the period 2000-2019 (**e**). Average values are presented in the lower left of each panel.

outside the atmospheric boundary layer). Therefore, changes in the degree of conservation of these semi-conserved parameters over time can be used as an indication of the impact of changes in the observation system on the dynamical consistency of the ERA5 dataset.

The ERA5 data assimilation time windows are 12 hours long and steps between these windows occur every day at 09:00 and 21:00 UTC. We measure the change within specific humidity, potential vorticity, and potential temperature of all particles between the start of each step, t_j (at 09:00 and 21:00 each day) and the following hour, t_{j+1} (at 10:00 and 22:00 each day) that are below 20 km. This gives us the absolute tracer conservation errors (ATCEs) (Stohl et al., 1998b) during assimilation time steps:

$$ATCE_a(\gamma) = \frac{1}{N_a N_{part}} \sum_{j=1}^{N_a} \sum_{i=1}^{N_{part}} |\gamma_i(t_{j+1}) - \gamma_i(t_j)|, \tag{1}$$

where γ_i is the semi-conserved property of particle i at time t_j, N_{part} is the total number of particles considered, and N_a are the total number of assimilation time steps in the selected time range. As mentioned above, these properties are not perfectly conserved in the atmosphere, given that air masses are subject to a multitude of physical processes resulting in changes. Furthermore, errors in trajectory calculation other than those resulting from data assimilation as well as the interpolation of the semi-conserved quantities themselves produce conservation errors. Therefore, to measure the degree of trajectory inaccuracy resulting from data assimilation in ERA5, it is necessary to establish a baseline. We define this baseline as the average of the hour before and after the assimilation time step:

$$ATCE_b(\gamma) = \frac{1}{2N_a N_{part}} \sum_{j=1}^{N_a} \sum_{i=1}^{N_{part}} |\gamma_i(t_{j+2}) - \gamma_i(t_{j+1})| + |\gamma_i(t_j) - \gamma_i(t_{j-1})|, \tag{2}$$

We note that the $ATCE_b$ values are always smaller than the $ATCE_a$ values and show no substantial temporal trends (not shown). We therefore measure the effect of the data assimilation on the dynamical consistency of meteorological fields by subtracting the baseline conservation error from the conservation error during the data assimilation:

$$ATCE_c(\gamma) = ATCE_a(\gamma) - ATCE_b(\gamma) \tag{3}$$

The resulting $ATCE_c$ values show substantial changes over time. Figure 5 shows both the full 84-year period trend of $ATCE_c$ for specific humidity, potential vorticity and potential temperature, as well as the spatial global distribution of $ATCE_c$ values for potential temperature. Assimilation discontinuities are generally the lowest in the early 1940s, when observations were scarce and the IFS model was only weakly constrained. They then grow until 1978, when progressively more observations were assimilated. However, striking is the steep drop in tracer conservation discontinuities after 1978. For potential vorticity and potential temperature, this drop originates mostly from changes in the Southern Hemisphere, where the largest increase in observation data occurred. This is in line with the introduction of assimilation of ~~data~~ satellite data, such as from the TOVS (TIROS Operational Vertical Sounder) satellite series at the end of 1978 (Bell et al., 2021). An increase in the quantity of observational data, and thus a stronger observational constraint, therefore not necessarily causes a degradation in tracer conservation. We have highlighted the period prior to this drop, when discontinuities due to data assimilation were at their

highest, by mapping the potential temperature discontinuities on a 2° by 2° grid (Figure 5d). Assimilation discontinuities in the Southern Hemisphere are strongly concentrated in certain regions and are, overall, much larger than in the Northern Hemisphere in the period before 1979 (Figure 5d), even though before 1979 data availability in the Southern Hemisphere was much more sparse than in the Northern Hemisphere (Soci et al., 2024). It seems that assimilation of the few localized observations in the Southern Hemisphere, as visible in Figure 1 of Soci et al. (2024), caused large changes in the model state. This is particularly evident over South America and the Antarctic Peninsula, where land-based observations were available. In the Northern Hemisphere, $ATCE_c$ values for potential temperature are more evenly distributed over the whole domain. After 1979, the situation becomes similar in the Southern Hemisphere as visible in Figure 5e. It is also interesting to see that $ATCE_c$ values for specific humidity increase throughout the ERA5 period, while $ATCE_c$ values for potential temperature remained nearly constant after 1979.

Similar results to the ones discussed above could be obtained by analysing the change in the gridded ERA5 data before and after assimilation timesteps directly, but this would not include the information *along* the trajectories of air masses through space. Expanding on this example, it would be possible to trace particles selected from high-assimilation discontinuity regions and investigate which downstream regions are strongly affected by "shocks" induced by the data assimilation. Similarly, it would be possible to trace regions with known discrepancies in meteorological parameters backward in time to investigate where and when the affected air masses underwent strong changes in meteorological properties due to the data assimilation. Such studies could help identify problems in the data assimilation system.

5 Conclusions

This study presents LARA, a Lagrangian reanalysis dataset, and outlines its potential and limitations in studying atmospheric transport processes. The dataset was created using the latest version of FLEXPART (Bakels et al., 2024) with meteorological input data from the ERA5 reanalysis (Hersbach et al., 2020), and contains the hourly instantaneous and averaged values of positions, potential vorticity, specific humidity, density, temperature, and pressure for six million particles over the past 84 years. If users require other meteorological variables, they could be interpolated, e.g., from gridded ERA5 data, to the particle positions in a post-processing step. The full dataset is divided in parts of eight years with a full year overlap between the periods. Within each eight-year period, particle trajectories are continuous and particles are distributed homogeneously in the whole atmosphere. We show that the particle distribution in the troposphere approximately fulfills the well-mixed condition, i.e. the distribution of particles in the troposphere shows relatively small deviations from the distribution of air density throughout the whole period. Small deviations of $< 6.6\%$ indicate potential for further improvements but should not limit the usability of the LARA dataset for most conceivable applications. However, above the troposphere the errors are larger, and caution should to be taken when using LARA for stratospheric studies.

We provided four different examples, with the aim of demonstrating the wide range of applications for which LARA can be used. By selecting particles that cross the equator, and following these for 20 days forward, we used their distribution after

20 days to establish a measure of the Hadley cell transport. This revealed a strong link between the latitudinal extension of the particle distribution and the PDO index. In a similar way, particles could be selected and traced within the past 84 years given any location. In our second example, the warm conveyor belt analysis, we showed the possibility of using LARA to find coherent air streams on the basis of dynamical trajectory criteria. We found shifts in the occurrence and intensity of these events over time, with implications for understanding the impact of climate variability on extreme weather events. Similarly, properties of the particles within WCBs could be analysed to better understand, for example, the relation between WCBs and potential vorticity. However, we caution users that the quality of LARA is determined by the underlying ERA5 data, and that care must to be taken when studying trends over periods that use different assimilation data. In our third example, we used LARA to obtain a Lagrangian definition of continentality. By tracking the time particles spend over land, we quantified how long it takes air to reach land from the ocean. This analysis could be expanded by additionally tracking moisture, e.g., using a moisture source diagnostic. In our last example, we showed that the LARA dataset can be used to diagnose properties in the ERA5 data. We highlighted how changes in the observation system and data assimilation procedures introduce dynamical inconsistencies that can be quantified using the LARA dataset. By examining the conservation of semi-conserved tracers, such as specific humidity, potential vorticity, and potential temperature, this study provides a means to assess the reliability of LARA data across different periods. It should be noted that the analytical purposes presented here are not intended to be all-encompassing.

Perhaps the largest limitation of the LARA data set is the modest number of particles tracked. This limits the effective time-space resolution of analyses, especially when it comes to case studies of individual events (e.g., extreme precipitation events). Perhaps LARA can trigger enough interest in the scientific community that future Lagrangian reanalyses will be carried out by meteorological centers with larger computational resources than those available at a university. This will facilitate the tracking and archiving of a much larger number of particles, and could include a more direct connection to the Eulerian reanalysis, facilitating the efficient provision of additional meteorological variables along the particle trajectories from within the same data archive.

Code and data availability. The dataset is hosted by the Earth Observation Data Center (EODC) and available to the public via: https://data.eodc.eu/collections/LARA/ as a Zarr dataset. LARA is produced using FLEXPART, available from https://doi.org/10.5281/zenodo.12706632 (Bakels et al., 2024). All scripts necessary to create the dataset, as well as the scripts to reproduce the analyses and plots in this work are provided in the Supplement. In addition, processed LARA data that were used to create the plots can be found here: https://doi.org/10.5281/zenodo.14639472.

Author contributions. LB created the dataset; validated the dataset; created most figures; and wrote the majority of the paper. MB managed the conversion to Zarr and the storage of the dataset; and provided text. MD, in collaboration with GB, created the section on the continentality of air; provided feedback and contributed to the text. AP contributed ideas, tested the dataset, and helped with the design of plots and text. VL contributed to the analysis of the validation and limitation of the dataset. GB, in collaboration with MD, analysed the continentality of

480 air using the LARA dataset. LH made hosting arrangement of the data and contributed textual feedback. AS provided ideas, feedback on the analysis, and contributed to the text.

Competing interests.   No competing interests

Acknowledgements.   We acknowledge valuable input from Michael Meyer, Sabine Eckhardt, and Katharina Baier. We acknowledge the Earth Observation Data Center (EODC) for storing and distributing the data using their facilities. This study has been supported by the Dr. Gottfried
485 and Dr. Vera Weiss Science Foundation and the Austrian Science Fund in the framework of the project no. P 34170-N, "A demonstration of a Lagrangian re-analysis (LARA)". The computational results presented have been achieved using the Vienna Scientific Cluster (VSC). In addition, we acknowledge various public Python packages that have benefited our study: NumPy (Harris et al., 2020), Matplotlib (Hunter, 2007), Xarray (Hoyer and Hamman, 2017), SciPy (Virtanen et al., 2020), and cartopy (Met Office, 2010 - 2015).

References

Arnold, D., Maurer, C., Wotawa, G., Draxler, R., Saito, K., and Seibert, P.: Influence of the meteorological input on the atmospheric transport modelling with FLEXPART of radionuclides from the Fukushima Daiichi nuclear accident, Journal of Environmental Radioactivity, 139, 212–225, https://doi.org/10.1016/j.jenvrad.2014.02.013, 2015.

Baier, K., Duetsch, M., Mayer, M., Bakels, L., Haimberger, L., and Stohl, A.: The Role of Atmospheric Transport for El Niño-Southern Oscillation Teleconnections, Geophysical Research Letters, 49, e2022GL100 906, https://doi.org/10.1029/2022GL100906, 2022.

Bakels, L., Tatsii, D., Tipka, A., Thompson, R., Dütsch, M., Blaschek, M., Seibert, P., Baier, K., Bucci, S., Cassiani, M., Eckhardt, S., Groot Zwaaftink, C., Henne, S., Kaufmann, P., Lechner, V., Maurer, C., Mulder, M. D., Pisso, I., Plach, A., Subramanian, R., Vojta, M., and Stohl, A.: FLEXPART version 11: improved accuracy, efficiency, and flexibility, Geoscientific Model Development, 17, 7595–7627, https://doi.org/10.5194/gmd-17-7595-2024, 2024.

Beck, H. E., McVicar, T. R., Vergopolan, N., Berg, A., Lutsko, N. J., Dufour, A., Zeng, Z., Jiang, X., van Dijk, A. I., and Miralles, D. G.: High-resolution (1 km) Köppen-Geiger maps for 1901–2099 based on constrained CMIP6 projections, Scientific data, 10, 724, https://doi.org/10.1038/s41597-023-02549-6, 2023.

Bell, B., Hersbach, H., Simmons, A., Berrisford, P., Dahlgren, P., Horányi, A., Muñoz-Sabater, J., Nicolas, J., Radu, R., Schepers, D., Soci, C., Villaume, S., Bidlot, J.-R., Haimberger, L., Woollen, J., Buontempo, C., and Thépaut, J.-N.: The ERA5 global reanalysis: Preliminary extension to 1950, Quarterly Journal of the Royal Meteorological Society, 147, 4186–4227, https://doi.org/https://doi.org/10.1002/qj.4174, 2021.

Cassiani, M., Stohl, A., and Brioude, J.: Lagrangian stochastic modelling of dispersion in the convective boundary layer with skewed turbulence conditions and a vertical density gradient: Formulation and implementation in the FLEXPART model, Boundary-Layer Meteorology, 154, 367–390, https://doi.org/10.1007/s10546-014-9976-5, 2015.

Chen, B., Xu, X.-D., Yang, S., and Zhang, W.: On the origin and destination of atmospheric moisture and air mass over the Tibetan Plateau, Theoretical and Applied Climatology, 110, 423–435, https://doi.org/10.1007/s00704-012-0641-y, 2012.

Courtier, P. and Talagrand, O.: Variational Assimilation of Meteorological Observations With the Adjoint Vorticity Equation. Ii: Numerical Results, Quarterly Journal of the Royal Meteorological Society, 113, 1329–1347, https://doi.org/https://doi.org/10.1002/qj.49711347813, 1987.

Dirmeyer, P. A. and Brubaker, K. L.: Contrasting evaporative moisture sources during the drought of 1988 and the flood of 1993, Journal of Geophysical Research: Atmospheres, 104, 19 383–19 397, https://doi.org/10.1029/1999JD900222, 1999.

Eckhardt, S., Stohl, A., Wernli, H., James, P., Forster, C., and Spichtinger, N.: A 15-Year Climatology of Warm Conveyor Belts, Journal of Climate, 17, 218 – 237, https://doi.org/10.1175/1520-0442(2004)017<0218:AYCOWC>2.0.CO;2, 2004.

Enfield, D. B., Mestas-Nuñez, A. M., and Trimble, P. J.: The Atlantic Multidecadal Oscillation and its relation to rainfall and river flows in the continental U.S., Geophysical Research Letters, 28, 2077–2080, https://doi.org/https://doi.org/10.1029/2000GL012745, 2001.

Flaounas, E., Kotroni, V., Lagouvardos, K., Gray, S. L., Rysman, J.-F., and Claud, C.: Heavy rainfall in Mediterranean cyclones. Part I: contribution of deep convection and warm conveyor belt, Climate dynamics, 50, 2935–2949, https://doi.org/10.1007/s00382-017-3783-x, 2018.

Fremme, A. and Sodemann, H.: The role of land and ocean evaporation on the variability of precipitation in the Yangtze River valley, Hydrology and Earth System Sciences, 23, 2525–2540, https://doi.org/10.5194/hess-23-2525-2019, 2019.

Fujiwara, M., Wright, J. S., Manney, G. L., Gray, L. J., Anstey, J., Birner, T., Davis, S., Gerber, E. P., Harvey, V. L., Hegglin, M. I., Homeyer, C. R., Knox, J. A., Krüger, K., Lambert, A., Long, C. S., Martineau, P., Molod, A., Monge-Sanz, B. M., Santee, M. L., Tegtmeier, S., Chabrillat, S., Tan, D. G. H., Jackson, D. R., Polavarapu, S., Compo, G. P., Dragani, R., Ebisuzaki, W., Harada, Y., Kobayashi, C., McCarty, W., Onogi, K., Pawson, S., Simmons, A., Wargan, K., Whitaker, J. S., and Zou, C.-Z.: Introduction to the SPARC Reanalysis Intercomparison Project (S-RIP) and overview of the reanalysis systems, Atmospheric Chemistry and Physics, 17, 1417–1452, https://doi.org/10.5194/acp-17-1417-2017, 2017.

Gelaro, R., McCarty, W., Suárez, M. J., Todling, R., Molod, A., Takacs, L., Randles, C. A., Darmenov, A., Bosilovich, M. G., Reichle, R., Wargan, K., Coy, L., Cullather, R., Draper, C., Akella, S., Buchard, V., Conaty, A., da Silva, A. M., Gu, W., Kim, G.-K., Koster, R., Lucchesi, R., Merkova, D., Nielsen, J. E., Partyka, G., Pawson, S., Putman, W., Rienecker, M., Schubert, S. D., Sienkiewicz, M., and Zhao, B.: The Modern-Era Retrospective Analysis for Research and Applications, Version 2 (MERRA-2), Journal of Climate, 30, 5419 – 5454, https://doi.org/10.1175/JCLI-D-16-0758.1, 2017.

Gimeno, L., Drumond, A., Nieto, R., Trigo, R. M., and Stohl, A.: On the origin of continental precipitation, Geophysical Research Letters, 37, https://doi.org/10.1029/2010GL043712, 2010.

Grise, K. M. and Davis, S. M.: Hadley cell expansion in CMIP6 models, Atmospheric Chemistry and Physics, 20, 5249–5268, https://doi.org/10.5194/acp-20-5249-2020, 2020.

Hakim, G. J., Emile-Geay, J., Steig, E. J., Noone, D., Anderson, D. M., Tardif, R., Steiger, N., and Perkins, W. A.: The last millennium climate reanalysis project: Framework and first results, Journal of Geophysical Research: Atmospheres, 121, 6745–6764, https://doi.org/https://doi.org/10.1002/2016JD024751, 2016.

Harris, C. R., Millman, K. J., van der Walt, S. J., Gommers, R., Virtanen, P., Cournapeau, D., Wieser, E., Taylor, J., Berg, S., Smith, N. J., Kern, R., Picus, M., Hoyer, S., van Kerkwijk, M. H., Brett, M., Haldane, A., del Río, J. F., Wiebe, M., Peterson, P., Gérard-Marchant, P., Sheppard, K., Reddy, T., Weckesser, W., Abbasi, H., Gohlke, C., and Oliphant, T. E.: Array programming with NumPy, Nature, 585, 357–362, https://doi.org/10.1038/s41586-020-2649-2, 2020.

Hersbach, H., Bell, B., Berrisford, P., Hirahara, S., Horányi, A., Muñoz-Sabater, J., Nicolas, J., Peubey, C., Radu, R., Schepers, D., et al.: The ERA5 global reanalysis, Quarterly Journal of the Royal Meteorological Society, 146, 1999–2049, https://doi.org/10.1002/qj.3803, 2020.

Hoyer, S. and Hamman, J.: xarray: N-D labeled arrays and datasets in Python, Journal of Open Research Software, 5, https://doi.org/10.5334/jors.148, 2017.

Hu, Y., Huang, H., and Zhou, C.: Widening and weakening of the Hadley circulation under global warming, Science Bulletin, 63, 640–644, https://doi.org/https://doi.org/10.1016/j.scib.2018.04.020, 2018.

Hunter, J. D.: Matplotlib: A 2D graphics environment, Computing in Science & Engineering, 9, 90–95, https://doi.org/10.1109/MCSE.2007.55, 2007.

Kobayashi, S., Ota, Y., Harada, Y., Ebita, A., Moriya, M., Onoda, H., Onogi, K., Kamahori, H., Kobayashi, C., Endo, H., Miyaoka, K., and Takahashi, K.: The JRA-55 Reanalysis: General Specifications and Basic Characteristics, Journal of the Meteorological Society of Japan. Ser. II, 93, 5–48, https://doi.org/10.2151/jmsj.2015-001, 2015.

KOSAKA, Y., KOBAYASHI, S., HARADA, Y., KOBAYASHI, C., NAOE, H., YOSHIMOTO, K., HARADA, M., GOTO, N., CHIBA, J., MIYAOKA, K., SEKIGUCHI, R., DEUSHI, M., KAMAHORI, H., NAKAEGAWA, T., TANAKA, T. Y., TOKUHIRO, T., SATO, Y., MATSUSHITA, Y., and ONOGI, K.: The JRA-3Q Reanalysis, Journal of the Meteorological Society of Japan. Ser. II, 102, 49–109, https://doi.org/10.2151/jmsj.2024-004, 2024.

Köppen, W.: Versuch einer Klassifikation der Klimate, vorzugsweise nach ihren Beziehungen zur Pflanzenwelt, Geographische Zeitschrift, 6, 593–611, http://www.jstor.org/stable/27803924, 1900.

Läderach, A. and Sodemann, H.: A revised picture of the atmospheric moisture residence time, Geophysical Research Letters, 43, 924–933, 2016.

Madonna, E., Wernli, H., Joos, H., and Martius, O.: Warm Conveyor Belts in the ERA-Interim Dataset (1979–2010). Part I: Climatology and Potential Vorticity Evolution, Journal of Climate, 27, 3 – 26, https://doi.org/10.1175/JCLI-D-12-00720.1, 2014.

Met Office: Cartopy: a cartographic python library with a Matplotlib interface, Exeter, Devon, https://scitools.org.uk/cartopy, 2010 - 2015.

Nieto, R., Gimeno, L., and Trigo, R. M.: A Lagrangian identification of major sources of Sahel moisture, Geophysical Research Letters, 33, https://doi.org/10.1029/2006GL027232, 2006.

Petterssen, S.: Weather analysis and forecasting: a textbook on synoptic meteorology, McGraw-Hill Book Company, 1940.

Pisso, I., Sollum, E., Grythe, H., Kristiansen, N. I., Cassiani, M., Eckhardt, S., Arnold, D., Morton, D., Thompson, R. L., Groot Zwaaftink, C. D., et al.: The Lagrangian particle dispersion model FLEXPART version 10.4, Geoscientific Model Development, 12, 4955–4997, https://doi.org/10.5194/gmd-12-4955-2019, 2019.

Reithmeier, C. and Sausen, R.: ATTILA: atmospheric tracer transport in a Lagrangian model, Tellus B: Chemical and Physical Meteorology, 54, 278–299, https://doi.org/10.3402/tellusb.v54i3.16666, 2002.

Rienecker, M. M., Suarez, M. J., Gelaro, R., Todling, R., Bacmeister, J., Liu, E., Bosilovich, M. G., Schubert, S. D., Takacs, L., Kim, G.-K., Bloom, S., Chen, J., Collins, D., Conaty, A., da Silva, A., Gu, W., Joiner, J., Koster, R. D., Lucchesi, R., Molod, A., Owens, T., Pawson, S., Pegion, P., Redder, C. R., Reichle, R., Robertson, F. R., Ruddick, A. G., Sienkiewicz, M., and Woollen, J.: MERRA: NASA's Modern-Era Retrospective Analysis for Research and Applications, Journal of Climate, 24, 3624 – 3648, https://doi.org/10.1175/JCLI-D-11-00015.1, 2011.

Saha, S., Moorthi, S., Pan, H.-L., Wu, X., Wang, J., Nadiga, S., Tripp, P., Kistler, R., Woollen, J., Behringer, D., Liu, H., Stokes, D., Grumbine, R., Gayno, G., Wang, J., Hou, Y.-T., ya Chuang, H., Juang, H.-M. H., Sela, J., Iredell, M., Treadon, R., Kleist, D., Delst, P. V., Keyser, D., Derber, J., Ek, M., Meng, J., Wei, H., Yang, R., Lord, S., van den Dool, H., Kumar, A., Wang, W., Long, C., Chelliah, M., Xue, Y., Huang, B., Schemm, J.-K., Ebisuzaki, W., Lin, R., Xie, P., Chen, M., Zhou, S., Higgins, W., Zou, C.-Z., Liu, Q., Chen, Y., Han, Y., Cucurull, L., Reynolds, R. W., Rutledge, G., and Goldberg, M.: The NCEP Climate Forecast System Reanalysis, Bulletin of the American Meteorological Society, 91, 1015 – 1058, https://doi.org/10.1175/2010BAMS3001.1, 2010.

Soci, C., Hersbach, H., Simmons, A., Poli, P., Bell, B., Berrisford, P., Horányi, A., Muñoz-Sabater, J., Nicolas, J., Radu, R., Schepers, D., Villaume, S., Haimberger, L., Woollen, J., Buontempo, C., and Thépaut, J.-N.: The ERA5 global reanalysis from 1940 to 2022, Quarterly Journal of the Royal Meteorological Society, n/a, 1–35, https://doi.org/10.1002/qj.4803, 2024.

Sodemann, H., Schwierz, C., and Wernli, H.: Interannual variability of Greenland winter precipitation sources: Lagrangian moisture diagnostic and North Atlantic Oscillation influence, Journal of Geophysical Research: Atmospheres, 113, https://doi.org/10.1029/2007JD008503, 2008.

Sprenger, M. and Wernli, H.: A northern hemispheric climatology of cross-tropopause exchange for the ERA15 time period (1979–1993), Journal of Geophysical Research: Atmospheres, 108, https://doi.org/10.1029/2002JD002636, 2003.

Stachnik, J. P. and Schumacher, C.: A comparison of the Hadley circulation in modern reanalyses, Journal of Geophysical Research: Atmospheres, 116, https://doi.org/https://doi.org/10.1029/2011JD016677, 2011.

Sterl, A.: On the (In)Homogeneity of Reanalysis Products, Journal of Climate, 17, 3866 – 3873, https://doi.org/10.1175/1520-0442(2004)017<3866:OTIORP>2.0.CO;2, 2004.

Stohl, A.: Computation, accuracy and applications of trajectories—A review and bibliography, Atmospheric Environment, 32, 947–966, https://doi.org/10.1016/S1352-2310(97)00457-3, 1998.

Stohl, A.: A 1-year Lagrangian "climatology" of airstreams in the northern hemisphere troposphere and lowermost stratosphere, Journal of Geophysical Research: Atmospheres, 106, 7263–7279, https://doi.org/https://doi.org/10.1029/2000JD900570, 2001.

Stohl, A. and James, P.: A Lagrangian analysis of the atmospheric branch of the global water cycle. Part I: Method description, validation, and demonstration for the August 2002 flooding in central Europe, Journal of Hydrometeorology, 5, 656–678, https://doi.org/10.1175/1525-7541(2004)005<0656:ALAOTA>2.0.CO;2, 2004.

Stohl, A. and James, P.: A Lagrangian Analysis of the Atmospheric Branch of the Global Water Cycle. Part II: Moisture Transports between Earth's Ocean Basins and River Catchments, Journal of Hydrometeorology, 6, 961 – 984, https://doi.org/10.1175/JHM470.1, 2005.

Stohl, A., Hittenberger, M., and Wotawa, G.: Validation of the Lagrangian particle dispersion model FLEXPART against large-scale tracer experiment data, Atmospheric Environment, 32, 4245–4264, https://doi.org/10.1016/S1352-2310(98)00184-8, 1998a.

Stohl, A., Eckhardt, S., Forster, C., James, P., and Spichtinger, N.: On the pathways and timescales of intercontinental air pollution transport, Journal of Geophysical Research: Atmospheres, 107, ACH 6–1–ACH 6–17, https://doi.org/10.1029/2001JD001396, 2002.

Stohl, A., Wernli, H., James, P., Bourqui, M., Forster, C., Liniger, M. A., Seibert, P., and Sprenger, M.: A New Perspective of Stratosphere–Troposphere Exchange, Bulletin of the American Meteorological Society, 84, 1565 – 1574, https://doi.org/10.1175/BAMS-84-11-1565, 2003.

Stohl, A., Forster, C., Frank, A., Seibert, P., and Wotawa, G.: The Lagrangian particle dispersion model FLEXPART version 6.2, Atmospheric Chemistry and Physics, 5, 2461–2474, https://doi.org/10.5194/acp-5-2461-2005, 2005.

Stohl, A. et al.: Evaluation of trajectories calculated from ECMWF data against constant volume balloon flights during ETEX, Atmospheric Environment, 32, 4151–4156, https://doi.org/10.1016/S1352-2310(98)00185-X, 1998b.

Studholme, J. and Gulev, S.: Concurrent Changes to Hadley Circulation and the Meridional Distribution of Tropical Cyclones, Journal of Climate, 31, 4367 – 4389, https://doi.org/10.1175/JCLI-D-17-0852.1, 2018.

Tandon, N. F., Gerber, E. P., Sobel, A. H., and Polvani, L. M.: Understanding Hadley Cell Expansion versus Contraction: Insights from Simplified Models and Implications for Recent Observations, Journal of Climate, 26, 4304 – 4321, https://doi.org/10.1175/JCLI-D-12-00598.1, 2013.

Thomson, D.: Criteria for the selection of stochastic models of particle trajectories in turbulent flows, Journal of fluid mechanics, 180, 529–556, https://doi.org/10.1017/S0022112087001940, 1987.

Tipka, A., Haimberger, L., and Seibert, P.: Flex_extract v7.1.2 – a software package to retrieve and prepare ECMWF data for use in FLEXPART, Geoscientific Model Development, 13, 5277–5310, https://doi.org/https://doi.org/10.5194/gmd-13-5277-2020, publisher: Copernicus GmbH, 2020.

Vázquez, M., Alvarez-Socorro, G., Fernández-Alvarez, J. C., Nieto, R., and Gimeno, L.: Global FLEXPART-ERA5 simulations using 30 million atmospheric parcels since 1980, https://doi.org/10.5281/zenodo.13682647, 2024.

Virtanen, P., Gommers, R., Oliphant, T. E., Haberland, M., Reddy, T., Cournapeau, D., Burovski, E., Peterson, P., Weckesser, W., Bright, J., van der Walt, S. J., Brett, M., Wilson, J., Millman, K. J., Mayorov, N., Nelson, A. R. J., Jones, E., Kern, R., Larson, E., Carey, C. J., Polat, İ., Feng, Y., Moore, E. W., VanderPlas, J., Laxalde, D., Perktold, J., Cimrman, R., Henriksen, I., Quintero, E. A., Harris, C. R., Archibald, A. M., Ribeiro, A. H., Pedregosa, F., van Mulbregt, P., and SciPy 1.0 Contributors: SciPy 1.0: Fundamental Algorithms for Scientific Computing in Python, Nature Methods, 17, 261–272, https://doi.org/10.1038/s41592-019-0686-2, 2020.

Vogelezang, D. and Holtslag, A.: Evaluation and model impacts of alternative boundary-layer height formulations, Boundary-Layer Meteorology, 81, 245–269, https://doi.org/https://doi.org/10.1007/BF02430331, 1996.

Waugh, D. and Hall, T.: AGE OF STRATOSPHERIC AIR: THEORY, OBSERVATIONS, AND MODELS, Reviews of Geophysics, 40, 1–1–1–26, https://doi.org/https://doi.org/10.1029/2000RG000101, 2002.

Wernli, H. and Davies, H. C.: A Lagrangian-based analysis of extratropical cyclones. I: The method and some applications, Quarterly Journal of the Royal Meteorological Society, 123, 467–489, https://doi.org/10.1002/qj.49712353811, 1997a.

Wernli, H. and Davies, H. C.: A Lagrangian-based analysis of extratropical cyclones. I: The method and some applications, Quart. J. Roy. Meteor. Soc., 123, 467–489, 1997b.

Wernli, H., Dirren, S., Liniger, M. A., and Zillig, M.: Dynamical aspects of the life cycle of the winter storm 'Lothar' (24–26 December 1999), Quarterly Journal of the Royal Meteorological Society, 128, 405–429, https://doi.org/10.1256/003590002321042036, 2002.

Zaplotnik, , Pikovnik, M., and Boljka, L.: Recent Hadley Circulation Strengthening: A Trend or Multidecadal Variability?, Journal of Climate, 35, 4157 – 4176, https://doi.org/10.1175/JCLI-D-21-0204.1, 2022.

Zhang, Y., Wallace, J. M., and Battisti, D. S.: ENSO-like Interdecadal Variability: 1900–93, Journal of Climate, 10, 1004 – 1020, https://doi.org/10.1175/1520-0442(1997)010<1004:ELIV>2.0.CO;2, 1997.

Zschenderlein, P., Fink, A. H., Pfahl, S., and Wernli, H.: Processes determining heat waves across different European climates, Quarterly Journal of the Royal Meteorological Society, 145, 2973–2989, https://doi.org/10.1002/qj.3599, 2019.